



# Daytime-only-mean data can enhance understanding of land-atmosphere coupling

Zun Yin<sup>1</sup>, Kirsten Findell<sup>2</sup>, Paul Dirmeyer<sup>3</sup>, Elena Shevliakova<sup>2</sup>, Sergey Malyshev<sup>2</sup>, Khaled Ghannam<sup>1</sup>, Nina Raoult<sup>4</sup>, and Zhihong Tan<sup>1</sup>

<sup>1</sup>Program in Atmospheric and Oceanic Sciences, Princeton University, Princeton, 08540, New Jersey, USA

<sup>2</sup>Geophysical Fluid Dynamics Laboratory, NOAA/OAR, Princeton, 08540, New Jersey, USA

<sup>3</sup>Center for Ocean-Land-Atmosphere Studies, George Mason University, Fairfax, 22030, Virginia, USA

<sup>4</sup>Laboratoire des Sciences du Climat et de l'Environnement, IPSL, CNRS-CEA-UVSQ, Gif-sur-Yvette, 91191, Essonne, France

**Correspondence:** Zun Yin (zyin@princeton.edu)

**Abstract.** Land-atmosphere (L-A) interactions encompass the co-evolution of the land surface and overlying planetary boundary layer, primarily during daylight hours. However, many studies have been conducted using monthly or entire-day-mean time series due to the lack of sub-daily data. It has been unclear whether the inclusion of nighttime data alters the assessment of L-A coupling or obscures L-A interactive processes. To address this question, we generate monthly (M), entire-day-mean (E), and daytime-only-mean (D) data based on the ERA5 (5th European Centre for Medium-Range Weather Forecasts reanalysis) product, and evaluate the strength of L-A coupling through two-legged metrics, which partition the impact of the land states on surface fluxes (the land leg) from the impact of surface fluxes on the atmospheric states (the atmospheric leg). Here we show that the spatial patterns of strong L-A coupling regions among the M-, D- and E-based diagnoses can differ by as much as 84.8%. The signal loss from E- to M-based diagnoses is determined by the memory of local L-A states. The differences between E- and D-based diagnoses can be driven by physical mechanisms or the averaging algorithms. To improve understanding of L-A interactions, we call attention to the urgent need for more high-frequency data from both simulations and observations for relevant diagnoses. Regarding model outputs, two approaches are proposed to resolve the storage dilemma for high-frequency data: (1) integration of L-A metrics within Earth System Models, and (2) producing alternative daily datasets based on different averaging algorithms.

15

## 1 Introduction

Numerous studies have demonstrated the importance of land-atmosphere (L-A) interactions to the earth system (Findell et al., 2011; Hu et al., 2021; Klein and Taylor, 2020; Laguë et al., 2019; Taylor et al., 2012). Manifested by the mass and energy exchanges between the land surface and the planetary boundary layer (PBL), L-A interactions determine the evolution of the



20 convective system (Hu et al., 2021; Klein and Taylor, 2020) as well as the occurrence of convective rainfall (Taylor et al.,  
2012). From a climatic perspective, the coupling processes between the land and the atmosphere can accelerate the frequency  
and intensity of extreme events (Dirmeyer et al., 2021; Miralles et al., 2019; Schumacher et al., 2019; Zhou et al., 2021) and the  
shift of climate regimes (Berg et al., 2017; Findell et al., 2019) under global warming. To better understand L-A interactions,  
a suite of metrics has been proposed for characterizing specific physical processes across broad spatial and temporal scales  
25 (Santanello et al., 2018). These metrics can reveal essential behaviors of L-A interactions and enhance our understanding of the  
coupling mechanisms (e.g., (Chen and Dirmeyer, 2017; Findell et al., 2011; Hu et al., 2021; Jach et al., 2022)). Additionally,  
they provide a benchmark to evaluate the performance of earth system models in simulating L-A coupling processes (e.g.,  
(Dirmeyer et al., 2018; Ferguson et al., 2012; Koster et al., 2006; Santanello et al., 2009)).

However, L-A interactions alone are not always the primary determinant in the climate system (Koster et al., 2004). To  
30 reveal hotspots where and when L-A interactions play an important role, two criteria have been proposed: 1) the state of the  
atmosphere must be highly responsive to variations in land properties, and 2) there must be physically meaningful variability  
in those land properties over time (Dirmeyer, 2011; Guo et al., 2006; Koster et al., 2004). Dirmeyer (2011) proposed a metric  
( $M$ ) to characterize both features as

$$M = \frac{db}{da} \cdot \sigma_a = \rho(a, b) \sigma_b. \quad (1)$$

35 The  $M$  contains two components to estimate the coupling strength between variables  $a$ , presumed to be the driver, and  $b$ , the  
response. The coupling is significant only when  $b$  is sensitive to  $a$  (high  $db/da$ ) and the variation of  $a$  (standard deviation  
of  $a$ ,  $\sigma_a$ ) is large. The formula is equivalent to the correlation coefficient between  $a$  and  $b$  (i.e.,  $\rho(a, b)$ ) multiplied by  $\sigma_b$ .  
The advantage of this metric is its vast suitability in characterizing coupling mechanisms across different scales (Chen and  
Dirmeyer, 2017; Guillod et al., 2014; Findell et al., 2011; Hu et al., 2021; Lorenz et al., 2015) regardless of specific variables.  
40 In terms of L-A interactions, Dirmeyer et al. (2014) divided the coupling linkage into two steps: the coupling between the land  
surface and surface fluxes of heat, moisture, or momentum, called the land leg, and the coupling between the surface fluxes  
and the atmosphere states, called the atmospheric leg (see Sect. 2.2).

The two-legged metrics (TLMs) mainly focus on relevant processes during the daytime. However, data covering the same  
time window is rare in available datasets. Consequently, most TLM research has been based on time series of monthly or  
45 24-hour average quantities (e.g., Dirmeyer et al. (2014); Hu et al. (2021); Lorenz et al. (2015)). Although these studies enhance  
our understanding of the patterns and seasonality of L-A coupling, it has yet to be shown whether the monthly- and entire-  
day-based inputs are able to capture areas with strong daytime land-atmosphere coupling accurately. In other words, are there  
significant differences among monthly-, entire-day-, and daytime-only-based L-A coupling diagnoses? If so, are the differences  
exclusively due to the averaging process, or are there other L-A coupling mechanisms that may mislead the diagnoses of  
50 daytime L-A coupling?

In this study, the  $0.25^\circ$  spatial resolution ERA5 (the fifth ECMWF ReAnalysis, (Hersbach et al., 2018)) is employed as  
the test bed to address these research questions. Three time series derived from ERA5 outputs, monthly-means (M), entire-  
day-means (E), and daytime-only-means (D), are utilized to calculate two-legged metrics (TLMs) to evaluate L-A coupling



strength. We investigate the spatial pattern differences among M-, E-, and D-based diagnoses. Primary contributors to the  
55 pattern mismatch are revealed, associated mechanisms are demonstrated, and implications are discussed.

## 2 Methods

### 2.1 ERA5 data

The ERA5 reanalysis provides 0.25°-hourly data determined through assimilation of observations (e.g., soil moisture, 10-  
m wind, 2-m humidity and temperature (Hersbach et al., 2020)). We collected ERA5 output every other hour from 1:00  
60 UTC (Coordinated Universal Time) 01-Jan-2011 until 23:00 UTC 31-Dec-2020 over  $[180^{\circ}\text{W}-180^{\circ}\text{E}] \times [65^{\circ}\text{S}-80^{\circ}\text{N}]$ . To be  
consistent with other daily data, the entire-day-mean values (E) are obtained by averaging time steps within each day based  
on the UTC. For the daytime-only-mean (D), the globe is divided into twenty-four time zones and the time is converted from  
UTC to LST (Local Solar Time). The time steps between 8am and 6pm LST are averaged to generate D values. The monthly  
mean (M) is a monthly average of E. To meet the minimum length requirement (Findell et al., 2015) for monthly TLMs  
65 estimations, we collected forty years of M data from 1981 through 2020. There are two chains in the L-A coupling process.  
One is how the land affects convective precipitation via latent heat flux. Another is how the land influences the growth of the  
Planetary Boundary Layer (PBL). As it is difficult to distinguish L-A triggered convective precipitation, we select the latter  
in this study including surface soil moisture from the 0–7 cm soil layer ( $\theta$  [ $\text{m}^3 \cdot \text{m}^{-3}$ ]) and sensible heat flux ( $H$  [ $\text{W} \cdot \text{m}^{-2}$ ]).  
Moreover, to implement ERA5 validation with ground-based observations (i.e., FLUXNET, validation results are not shown)  
70 that lacks observed PBL height, we select the pressure at the lifting condensation level ( $P_{\text{lcl}}$ ) to represent the atmospheric state,  
specifically that of the PBL, which can be estimated from three regular ground measurements: the surface pressure ( $P$  [Pa]),  
2-m temperature ( $T_{2\text{m}}$  [K]), and 2-m dew-point temperature ( $D_{2\text{m}}$  [K]) (Georgakakos and Bras, 1984), as:

$$P_{\text{lcl}} = P - P \left( \frac{T_{2\text{m}} - D_{2\text{m}}}{223.15} + 1 \right)^{-3.5}. \quad (2)$$

$P_{\text{lcl}}$  [Pa] is the pressure at LCL. The three time series are grouped by season. Both long-term trends and seasonality are removed  
75 to prevent them from obscuring the signal and altering the diagnoses.

### 2.2 Two-legged metrics

The two-legged metrics (TLMs) contain a land leg and an atmospheric leg to evaluate the two coupling links in the L-A  
interaction chain (Dirmeyer et al., 2014; Santanello et al., 2018). If  $\theta$ ,  $H$ , and  $P_{\text{lcl}}$  are utilized to represent the states of the land,  
the surface flux, and the atmosphere, the L-A coupling metrics (Eq. 1) can be formulated to assess the two-stepped coupling



80 processes as:

$$\begin{aligned}
 \mathcal{L} &= \frac{dH}{d\theta} \sigma_{\theta} = \rho(\theta, H) \cdot \sigma_H, \\
 \mathcal{A} &= \frac{dP_{\text{icl}}}{dH} \sigma_H = \rho(H, P_{\text{icl}}) \cdot \sigma_{P_{\text{icl}}}, \\
 \mathcal{T} &= \frac{dH}{d\theta} \frac{dP_{\text{icl}}}{dH} \sigma_{\theta} = \rho(\theta, H) \rho(H, P_{\text{icl}}) \cdot \sigma_{P_{\text{icl}}}.
 \end{aligned} \tag{3}$$

$\mathcal{L}$ ,  $\mathcal{A}$ , and  $\mathcal{T}$  indicate the land, the atmospheric, and the total legs, respectively. By applying to M, E, and D time series, we can get different versions of TLMs, denoted by  $\text{TLM}_M$ ,  $\text{TLM}_E$ , and  $\text{TLM}_D$ , respectively. For a specific variable and leg, we use M, E, and D as subscripts to distinguish them (e.g.,  $\mathcal{L}_M$ ,  $\mathcal{L}_E$ , and  $\mathcal{L}_D$ ).

### 2.3 Spatial pattern comparisons among M-, E-, and D-based diagnoses

It is not appropriate to directly compare the numerical values of TLMs based on different time windows of inputs (i.e., M, E, and D). First, the magnitude of the TLMs is strongly affected by the  $\sigma$  term (Eq. 1), and this measure of variability can be quite different for daytime and nighttime processes. For example,  $H_D$  has much larger variance than the  $H_E$ , which systematically enlarges the  $\mathcal{A}_D$ . Additionally, strong L-A coupling signals can be positive or negative, suggesting that in some cases the magnitude of TLM (its absolute value) is the relevant quantity of interest. Finally, L-A coupling processes are not characterized by clear thresholds, but rather by relative spatial and temporal differences. To overcome these limitations, we use quantile to assess coupling strengths and to quantify the differences among  $\text{TLM}_M$ ,  $\text{TLM}_E$ , and  $\text{TLM}_D$ . For a specific TLM and a given quantile threshold, regions with absolute values of TLM over this threshold are marked for the M, the D, and the E cases. For the  $\mathcal{A}_D$  in summer for example, if the given threshold was 0.8, grid cells with the top 20% largest  $|\mathcal{A}|$  are marked. The ratio of the number of overlapping grid cells to the number of E-based marked grid cells is defined as the fitting rate between  $\mathcal{A}_E$  and  $\mathcal{A}_D$ , which can reflect the difference between D- and E-based diagnoses at different levels of coupling strength. The same approach is applied to the legs in paired comparisons of E vs M, M vs D, and D vs E.

### 100 2.4 Signal attenuation from $\text{TLM}_E$ to $\text{TLM}_M$

According to our deduction (see Supplementary Text 1), we infer that the memory of the L-A state (i.e., the auto-correlation for a single variable and the cross-covariance for paired variables) can characterize the coupling signal attenuation due to the monthly smoothing of daily time series. Thus, for a single variable (i.e., the  $\sigma$  term), we calculate its auto-correlation function (ACF) with a maximum lag 30 days. Then we average the ACF values belonging to the top 25% quantile (Supplementary Fig. S7) as an indicator of the loss rate. And the attenuation rate is characterized by the ratio of  $\sigma_M$  to  $\sigma_E$ . For paired variables (i.e., the numerator of the  $\rho$  term  $N(\rho)$ ), we calculate the cross-covariance function (CCF) instead, but with a maximum lag  $\pm 30$  days. For negatively correlated variables, we select the mean of the lowest 25% CCF as the indicator. For positively correlated variables, we select top 25% as the quantile threshold as the ACF case. Instead of  $N(\rho_M)/N(\rho_E)$ , we use  $N(\rho_M)/(|N(\rho_E)| + |N(\rho_M)|)$  to characterize associated signal attenuation, in order to avoid uncertainties due to phase shift from  $N(\rho_E)$  to  $N(\rho_M)$ .



## 110 2.5 $\Delta|\text{TLM}|$ decomposition

According to the form of the coupling metrics (Eq. 1), the differences among  $|\text{TLM}_M|$ ,  $|\text{TLM}_E|$ , and  $|\text{TLM}_D|$  can be decomposed as:

$$\begin{aligned}\Delta|M| &= |M_2| - |M_1| \\ &= C_\rho + C_\sigma + C_{\sigma\rho}\end{aligned}$$

$$115 \quad C_\rho = \sigma_1 (|\rho_2| - |\rho_1|) \quad (4)$$

$$C_\sigma = |\rho_1| (\sigma_2 - \sigma_1)$$

$$C_{\sigma\rho} = (|\rho_2| - |\rho_1|) (\sigma_2 - \sigma_1).$$

$M_1$  and  $M_2$  are specific TLMs based on two different time series.  $\Delta|M|$  is the absolute value (coupling strength) shift from  $M_1$  to  $M_2$ , which is composed of contributions from the correlation term ( $C_\rho$ ), the fluctuation term ( $C_\sigma$ ), and the joint term  
 120 ( $C_{\sigma\rho}$ ). Note that the three terms may be either positive or negative. Thus, we take absolute values of them to estimate their contributions to the  $\Delta|M|$ . Taking the  $C_\rho$  as an example, its contribution is calculated as:

$$\frac{|C_\rho|}{|C_\rho| + |C_\sigma| + |C_{\sigma\rho}|}. \quad (5)$$

## 2.6 Primary contributors to TLM pattern shift

The shifts in spatial patterns from  $M_1$  to  $M_2$  can be characterized by the change of quantile ( $\Delta q$ ) rather than by the  $\Delta|\text{TLM}|$ ,  
 125 because the latter only quantifies the values of  $\Delta\text{TLM}$  within a specific grid cell, which cannot reflect the relative TLM change among grid cells. Moreover, within  $C_\rho$ ,  $C_\sigma$ , and  $C_{\sigma\rho}$ , the largest contributor (Eq. 4 and 5) to  $\Delta|\text{TLM}|$  may not be the dominant factor for  $\Delta q$  of specific grid cell. The dominant factor of a specific grid cell must be the one without which the quantile of the grid cell has the lowest change from  $\text{TLM}_1$  to  $\text{TLM}_2$ .

To demonstrate the dominant factor leading to  $\Delta q$  for a specific grid cell, we calculate  $\Delta q$  in four scenarios:

$$130 \quad \Delta q = q_{|M_2|} - q_{|M_1|}$$

$$\Delta q_{\rho^-} = q_{|M_2| - C_\rho} - q_{|M_1|}$$

$$\Delta q_{\sigma^-} = q_{|M_2| - C_\sigma} - q_{|M_1|}$$

$$\Delta q_{\sigma\rho^-} = q_{|M_2| - C_{\sigma\rho}} - q_{|M_1|}. \quad (6)$$

$\Delta q$  is the  $q$  shift of a specific grid cell from  $|M_1|$  to  $|M_2|$ .  $\Delta q_{\rho^-}$  is the  $q$  shift without the contribution of the  $\rho$  term (i.e., from  
 135  $|M_1|$  to  $|M_2| - C_\rho$ ). Similar definitions are applied for  $\Delta q_{\sigma^-}$  and  $\Delta q_{\sigma\rho^-}$ . Then we can demonstrate the dominant factor for a specific grid cell as:

$$f_{\min}(\Delta q_{\rho^-}, \Delta q_{\sigma^-}, \Delta q_{\sigma\rho^-}), \text{ if } \Delta q > 0,$$

$$f_{\max}(\Delta q_{\rho^-}, \Delta q_{\sigma^-}, \Delta q_{\sigma\rho^-}), \text{ if } \Delta q < 0. \quad (7)$$

$f_{\min}$  ( $f_{\max}$ ) is a function selecting the corresponding subscript of the term with the minimum (maximum) value.



## 140 3 Results

### 3.1 Spatial pattern differences among diagnoses based on $TLM_M$ , $TLM_E$ , and $TLM_D$

By using ERA5 hourly data, we generated three homologous time series by varied temporal averaging algorithms: monthly mean (M), entire-day-mean (E), and daytime-mean (D), which were used to estimate the coupling strength between land and atmosphere based on the two-legged metrics (Eq. 3, see Sect. 2.2). Figure 1 assesses the geographic consistency between the coupling strengths determined by the three different time series by showing the fitting rate of a suite of comparisons at different levels of quantile thresholds (see Sect. 2.3). The median of fitting rates over all legs and seasons is 69.4% if the largest 10% of TLM values are considered physically significant, demonstrating that the determination of L-A coupling strongly depends on the averaging time period of the input time series. Most fitting rates decrease with the rise of the quantile threshold, and the lowest fitting rate is 15.2% ( $\mathcal{A}_M$  vs.  $\mathcal{A}_D$  in JJA for the 0.95 quantile threshold), indicating that a minor portion of the most strongly coupled regions (the top 5%) are simultaneously diagnosed by both D and M. In all seasons,  $\mathcal{A}$  has a much lower fitting rate than  $\mathcal{L}$ , and the fitting rate of  $\mathcal{T}$  lies between the two. In addition, fitting rates are generally lower during JJA than in other seasons. Thus, to avoid a repetitive presentation of all results, we select  $\mathcal{A}$  in summer (JJA and DJF in the Northern and Southern Hemisphere, respectively) as an example to explore the TLM differences in the following content.

Figure 2a illustrates the differences of strong L-A coupling regions (90% quantile as the threshold) among  $\mathcal{A}_M$ ,  $\mathcal{A}_D$ , and  $\mathcal{A}_E$  during summer. Although the total overlap area ( $\mathcal{A}_M \cap \mathcal{A}_E \cap \mathcal{A}_D$ , pale taupe area in Fig. 2a) accounts for approximately 50% of strong coupling regions, vast disagreement among those diagnoses still exists especially in the Northern Hemisphere.  $\mathcal{A}_M$  suggests strong coupling in some climate transition regions (such as the western and southern US, central Asia, northern India, eastern Sahel, and southern Australia).  $\mathcal{A}_E$  highlights some mid-latitude regions, such as the southwestern and southeastern US, a part of the Sahara, Arabia, central India, and northwestern China. However, as the most accurate diagnosis,  $\mathcal{A}_D$  demonstrates that the L-A coupling is stronger in high latitudes, such as the boreal forest region of Canada, and parts of northern Eurasia. Interestingly, the fraction of  $\mathcal{A}_M \cap \mathcal{A}_D$  (1.7%) is much less than that of  $\mathcal{A}_M \cap \mathcal{A}_E$  (7.6%) or  $\mathcal{A}_E \cap \mathcal{A}_D$  (11.5%), implying that  $\mathcal{A}_E$  is the intermediate status between  $\mathcal{A}_M$  and  $\mathcal{A}_D$ . Therefore, we investigate the two-stepped transitions:  $\mathcal{A}_M \rightarrow \mathcal{A}_E$  (M vs E) and  $\mathcal{A}_E \rightarrow \mathcal{A}_D$  (E vs D) in the following analysis.

Figure 2b shows the quantile transition of  $\mathcal{A}_M \rightarrow \mathcal{A}_E$  in summer. Two types of regions are important. One is the green/yellow regions showing quantile shifts within the strongest coupling group, which coincide with Fig. 2a. The other is the dark blue/red regions, indicating the largest quantile changes from  $\mathcal{A}_M$  to  $\mathcal{A}_E$ . Interestingly, the quantile drops dramatically in the center of North America, the Sahel, and central Asia. On one hand, those  $\mathcal{A}_M$  diagnosed strongly L-A coupled regions agree with the findings from Koster et al. (2004) that was based on six-day averaged data. On the other hand, the coupling strength of those regions fades significantly when E-based diagnoses are applied. For instance, the quantile for three selected sites in these areas (red triangles in Fig. 2b) drops from  $> 80\%$  ( $\mathcal{A}_M$ ) to  $< 30\%$  ( $\mathcal{A}_E$ ). It indicates that the L-A coupling strength may be overestimated in those climatic transition zones if multi-day average data was applied. In the next section, we will demonstrate the mechanism resulting in such vast differences between  $\mathcal{A}_M$  and  $\mathcal{A}_E$ .



Figure 2c displays the quantile transition of  $\mathcal{A}_E \rightarrow \mathcal{A}_D$  in summer. In general, the most significant quantile shifts occur in the Northern Hemisphere and the strongly coupled regions are diagnosed further north by  $\mathcal{A}_D$ . The Sahara and Arabia contribute the largest quantile drop of  $\mathcal{A}_E \rightarrow \mathcal{A}_D$ . Some regions show strong coupling based on both  $\mathcal{A}_E$  and  $\mathcal{A}_D$ . However, their coupling strength is overestimated by  $\mathcal{A}_E$ , such as the southwestern US and northern Mexico, India, and northwestern China. Key regions with increasing  $\mathcal{A}$  quantile include the eastern US, boreal forests of Canada, northern Eurasia, and northeastern China.

### 3.2 M vs E

Through analyzing the formulas of  $TLM_E$  and  $TLM_M$  (see Supplementary Text 1), we demonstrate that both the  $\sigma$  term and the numerator of the  $\rho$  term (denoted by  $N(\rho)$ ) attenuate from  $TLM_E$  to  $TLM_M$ . The decreasing rate relies on the contrast between the variation of daily elements within the same month and the variation of daily elements across months. Furthermore, we infer that the memory of specific E time series (i.e.,  $\overline{ACF}_{>75\%}$ ) or paired E time series (i.e.,  $\overline{CCF}_{>75\%}$  and  $\overline{CCF}_{<25\%}$  for positively and negatively correlated pairs, respectively) can be an indicator characterizing the coupling signal loss from E to M (see Sect. 2.4).

Figure 3 verifies our deduction by showing high correlations between the coupling signal loss rate and the indicator regarding L-A memory. Significant correlation coefficients suggest that our indicator adequately explains the attenuation of the coupling signal due to monthly smoothing. Specifically, regions with higher auto-correlation between individual days lead to a smaller loss of information when a daily time series is converted to a monthly time series. In the negative pair case (Fig. 3d), the indicator sensitivity to the signal attenuation may be weakened. The primary distractors (top and bottom-right regions isolated by blue lines in Fig. 3d) are from areas with extreme climate conditions, such as Greenland, Sahara, and Arabia (Fig. 3f). Nevertheless, the moderately large correlation coefficient suggests that the indicator is still able to reflect the attenuation process. Surprisingly, the indicator captures not only the signal attenuation, but also phase shifts (the negative quadrant in Fig. 3e).

Through Figure 3, we demonstrate that  $TLM_M$  loses L-A coupling signal as a result of smoothing the E time series and the memory of L-A states determines the attenuation rate. Although memory is another facet of system coupling at the seasonal scale (Dirmeyer et al., 2009, 2016, 2018; Guo et al., 2011), it is not the main focus of TLM diagnosing the inter-daily L-A interactions. Moreover, two types of memories (auto-correlation of a single variable and cross-covariance of coupled variables, Supplementary Eq. S8 and S9) jointly influence the  $TLM_M$  in form of the quotient, which increases the uncertainty of  $TLM_M$  reflecting the signal of local L-A memory. Thus, we conclude that the diagnoses based on  $TLM_M$  are obscured by the varied memories of L-A state, which is not clearly represented in the  $TLM_M$  and is not the primary feature to be dug out.

### 3.3 E vs D

The value of  $|\mathcal{L}_D|$  is larger than  $|\mathcal{L}_E|$  worldwide (Supplementary Fig. S2a), and the primary contributor is the variability ( $C_\sigma$ , Fig. 4a, see Sect. ??). But the universal increase of  $C_\sigma$  is not always the key driver of spatial pattern differences between  $\mathcal{L}_E$  and  $\mathcal{L}_D$  (Fig. 4c). For instance, both  $\mathcal{L}_E$  and  $\mathcal{L}_D$  suggest a portion of middle and high latitude regions of the Northern Hemisphere with strong soil moisture-sensible heat flux ( $\theta-H$ ) coupling (Supplementary Fig. S3). However, different from



$\mathcal{L}_E$ ,  $\mathcal{L}_D$  suggests stronger coupling in North America than in Eurasia, which is primarily caused by the change of  $\rho$  ( $C_\rho$  and  $C_{\sigma\rho}$ ). This difference is caused by the time averaging algorithm of the E time series, which considers one day from 0:00 to 24:00 based on Coordinated Universal Time (UTC). Thus, the E averaging period in the Western Hemisphere starts at night and ends on the following day. The opposite is true for the Eastern Hemisphere (left panel of Fig. 4e). However, in a large  
210 region of North America, the nighttime soil moisture  $\theta_N$  is more correlated to the daytime soil moisture  $\theta_N$  of the previous day than the next day (Supplementary Fig. S5). Thus the entire-day average in the Western Hemisphere dramatically flattens the inter-daily fluctuations of soil moisture, leading to an underestimation of  $\rho(\theta, H)$  by E. The right panel of Figure 4e shows that in a selected area of North America, the difference between E- and D- based  $\rho(\theta, H)$  is significantly reduced if the  $\theta_E$  was calculated by averaging the  $\theta_D$  and the following  $\theta_N$ .

215 Figure 4b shows that both  $C_\sigma$  and the  $C_\rho$  can be important for  $\Delta|\mathcal{A}|$  from E to D.  $C_\sigma$  is likely the main contributor in humid regions, while the  $C_\rho$  dominates arid and semi-arid areas. Figure 4d illustrates that  $C_\sigma$  is the primary contributor to quantile increase in most strong  $\mathcal{A}$  regions (yellow areas in Figure 2c). However, in fact, their quantile increase is caused by the quantile decrease in the Sahara and Arabia (Supplementary Fig. S2b), where  $\mathcal{A}$  is negative (Supplementary second row of Fig. S4). As  $\mathcal{A}_D$  is universally higher than  $\mathcal{A}_E$ , the coupling strength over the Sahara and Arabia is weakened.

220 Generally, the land surface is the source of heating for the lower atmosphere during the day. Driven by the surface temperature  $T_s$ ,  $H$  heats the air and grows the height of the PBL (left panel of Fig. 4f), leading to positive  $\rho(H, T_{2m})$  and  $\rho(H, P_{1cl})$ . However, the climate of the Sahara and Arabia is likely dominated by another mechanism. Over the northern Sahara, for instance, atmospheric advection seems to be the primary driver of inter-daily variations of near-surface atmospheric states (i.e., both  $T_{2m}$  and  $D_{2m}$ ) instead of the surface (middle panel of Fig. 4f, see Supplementary Text 2). A key consequence is that the  
225  $T_{2m}$  is no longer a passive variable, but drives the  $H$  fluctuation (right panel of Fig. 4f), resulting in a negative  $\rho(H, T_{2m})$  and further a negative  $\rho(H, P_{1cl})$ . In fact, both the bottom-up heating and the advection-driven heating mechanisms (left and middle panel of Fig. 4f) affect the climate variations in this region. However, the former only occurs during the daytime, while the latter can exist throughout a day. In comparison to E, the D averaging approach can minimize the effect of the former in L-A diagnoses.

#### 230 4 Discussion

We demonstrate that the use of both monthly-mean and entire-day-mean daily data may result in biases in the diagnosis of L-A coupling. By comparing the two-legged metrics (TLM) calculated by the monthly (M), the daytime-only-mean (D), and entire-day-mean (E) time series, we found that the coverage discrepancy of their spatial patterns of strong coupling can be as large as 84.8% (Fig. 1). The diagnostic uncertainties introduced through monthly smoothing (i.e., differences between  $TLM_E$   
235 and  $TLM_M$ ) are determined by the persistence or memory of local L-A states, which may result in the overestimation of L-A coupling strength in some climatic transition zones (Koster et al., 2004). Furthermore, we have demonstrated that integrating nighttime information in L-A diagnoses (i.e.,  $TLM_E$ ) may incorporate confounding effects from other mechanisms.





Land-atmosphere interactions have been demonstrated to be a key element in understanding climate dynamics (Berg et al., 2017; Findell et al., 2015; Humphrey et al., 2021; Koster et al., 2004; Seneviratne et al., 2010; Taylor et al., 2012). Different  
240 from simple causality, the land and the atmosphere are highly coupled by multiple variables that interact with each other  
(Santanello et al., 2018; Seneviratne et al., 2010), which raises difficulties for the understanding and simulation of relevant  
processes (Taylor et al., 2012, 2017). To investigate the complex coupled system, we must characterize its behaviors under  
various conditions and reveal relevant physical processes. Thus, a suite of metrics has been proposed to detect the features of  
a specific process (Santanello et al., 2018) based on either physical or statistical perspectives ([https://www.pauldirmeyer.com/  
245 coupling-metrics](https://www.pauldirmeyer.com/coupling-metrics)). Moreover, these metrics are helpful to evaluate model performances either against observations or through  
model inter-comparisons, and further support model improvements. However, it is rare to find datasets providing the required  
complete fields of high-frequency ( $\leq 3$  hours) outputs for L-A investigations. For instance, daily data is generally the highest  
frequency output provided by numerous model inter-comparison projects (e.g., (Eyring et al., 2016; Warszawski et al., 2014)),  
which is not adequate to diagnose the performance of Earth system models (ESMs) in simulating L-A interactions. Moreover,  
250 our study demonstrates that even daily data may overlook some important L-A patterns due to the effects of other processes.  
The daytime-only-mean daily data used in our study is an average of time steps within the nine hours centered on local noon,  
whereas the traditional entire-day-mean daily data is obtained by averaging over 24 hours based on the UTC. Thus the latter  
emphasizes shifted diurnal cycles according to longitude, which may mask signals of land state fluctuation in the Western  
Hemisphere, and provide inconsistent comparisons with the Eastern Hemisphere.

255 Therefore, we call for careful attention to the requirements of high-frequency data in terms of diurnal cycle investigations,  
whose diagnoses can further reinforce ESM skills in predicting future climate under different scenarios. Assuredly, storage is a  
bottleneck for producing and sharing high-frequency data. Thus, we propose two approaches to balance the cost of storage and  
the need for high-frequency data. One approach is to integrate process-based metrics within ESMs so that the metric values  
themselves can be saved as model output, rather than calculated *a posteriori* (Findell and Eltahir, 2003a, b; Santanello et al.,  
260 2009; Tawfik and Dirmeyer, 2014). Therefore the diagnosis information can be easily collected at the cost of only a little extra  
computing time. The other is to generate different types of daily model output for different research purposes. In addition to  
daytime mean values, separate averages throughout the local morning, afternoon, and nighttime would be interesting as well  
(Taylor et al., 2012; Guillod et al., 2015). Such averaging algorithms must depend on the local time rather than the UTC, and  
the varied daytime length according to latitude and time of year should be considered.

## 265 5 Conclusions

This study demonstrates that the use of monthly or entire-day-mean daily data may lead to uncertainties in diagnoses of land-  
atmosphere (L-A) coupling strength and interactions. The arithmetic mean of time series including the nighttime weakens the  
signal of L-A coupling. And the spatial heterogeneity of such weakening effects can alter the diagnosis of coupling strength  
based on the two-legged metrics. In addition, two phenomena were discovered, which can dramatically obscure the L-A di-  
270 agnoses if the entire-day-mean daily time series is applied. Through this study, we call for attention to the requirements of



high-frequency data for L-A diagnoses. L-A metrics can be either integrated within Earth System Models to avoid huge storage for high-frequency outputs or fed by outputs averaging over the sub-daily period of interest. Either of the approaches can improve the accuracy of L-A diagnoses with minimal cost of computing time and storage space.

*Code and data availability.* The 0.5° ERA5 data is available at <https://cds.climate.copernicus.eu/#!/home>. The code for calculating the two-  
275 legged metrics can be found via <http://www.coupling-metrics.com>.

*Author contributions.* Z.Y., K.F., E.S., and S.M. conceived the research; Z.Y. and K.F. designed research; Z.Y. and N.R. collected and processed the data; Z.Y. performed research; Z.Y. draft the manuscript; all authors interpreted results and contributed to the editing.

*Competing interests.* The authors declare no competing interests.

*Acknowledgements.* Z.Y. and K.F. are supported by CIMES grant NA18OAR4320123. P.D. is supported by NOAA grant NA19OAR4310242.  
280 Yujin Zeng and Jing Feng are acknowledged for their comments and suggestions on an internal review of the manuscript. We acknowledge GFDL resources made available for this research. We thank the European Centre for Medium-Range Weather Forecasts (ECMWF) for providing the ERA5 data.



## References

- Berg, A., Lintner, B., Findell, K., and Giannini, A.: Soil Moisture Influence on Seasonality and Large-Scale Circulation in Simulations of the  
285 West African Monsoon, *Journal of Climate*, 30, 2295–2317, <https://doi.org/10.1175/JCLI-D-15-0877.1>, 2017.
- Chen, L. and Dirmeyer, P. A.: Impacts of Land-Use/Land-Cover Change on Afternoon Precipitation over North America, *Journal of Climate*,  
30, 2121–2140, <https://doi.org/10.1175/JCLI-D-16-0589.1>, 2017.
- Dirmeyer, P. A.: The terrestrial segment of soil moisture-climate coupling, *Geophysical Research Letters*, 38, n/a–n/a,  
<https://doi.org/10.1029/2011GL048268>, 2011.
- 290 Dirmeyer, P. A., Schlosser, C. A., and Brubaker, K. L.: Precipitation, recycling, and land memory: An integrated analysis, *Journal of Hy-*  
*drometeorology*, 10, 278–288, <https://doi.org/10.1175/2008JHM1016.1>, 2009.
- Dirmeyer, P. A., Wang, Z. Y., Mbuh, M. J., and Norton, H. E.: Intensified land surface control on boundary layer growth in a changing  
climate, *Geophysical Research Letters*, 41, 1290–1294, <https://doi.org/10.1002/2013GL058826>, 2014.
- Dirmeyer, P. A., Wu, J., Norton, H. E., Dorigo, W. A., Quiring, S. M., Ford, T. W., Santanello, J. A., Bosilovich, M. G., Ek, M. B., Koster,  
295 R. D., Balsamo, G., and Lawrence, D. M.: Confronting Weather and Climate Models with Observational Data from Soil Moisture Networks  
over the United States, *Journal of Hydrometeorology*, 17, 1049–1067, <https://doi.org/10.1175/JHM-D-15-0196.1>, 2016.
- Dirmeyer, P. A., Chen, L., Wu, J., Shin, C. S., Huang, B., Cash, B. A., Bosilovich, M. G., Mahanama, S., Koster, R. D., Santanello, J. A., Ek,  
M. B., Balsamo, G., Dutra, E., and Lawrence, D. M.: Verification of land-atmosphere coupling in forecast models, reanalyses, and land  
surface models using flux site observations, *Journal of Hydrometeorology*, 19, 375–392, <https://doi.org/10.1175/JHM-D-17-0152.1>, 2018.
- 300 Dirmeyer, P. A., Balsamo, G., Blyth, E. M., Morrison, R., and Cooper, H. M.: Land-Atmosphere Interactions Exacerbated the Drought and  
Heatwave Over Northern Europe During Summer 2018, *AGU Advances*, 2, <https://doi.org/10.1029/2020av000283>, 2021.
- Eyring, V., Bony, S., Meehl, G. A., Senior, C. A., Stevens, B., Stouffer, R. J., and Taylor, K. E.: Overview of the Coupled Model  
Intercomparison Project Phase 6 (CMIP6) experimental design and organization, *Geoscientific Model Development*, 9, 1937–1958,  
<https://doi.org/10.5194/gmd-9-1937-2016>, 2016.
- 305 Ferguson, C. R., Wood, E. F., and Vinukollu, R. K.: A Global intercomparison of modeled and observed land-atmosphere coupling, *Journal*  
*of Hydrometeorology*, 13, 749–784, <https://doi.org/10.1175/JHM-D-11-0119.1>, 2012.
- Findell, K. L. and Eltahir, E. A. B.: Atmospheric Controls on Soil Moisture–Boundary Layer Interactions. Part I: Framework Development,  
*Journal of Hydrometeorology*, 4, 552–569, [https://doi.org/10.1175/1525-7541\(2003\)004<0552:ACOSML>2.0.CO;2](https://doi.org/10.1175/1525-7541(2003)004<0552:ACOSML>2.0.CO;2), 2003a.
- Findell, K. L. and Eltahir, E. A. B.: Atmospheric controls on soil moisture-boundary layer interactions: Three-dimensional wind effects,  
310 *Journal of Geophysical Research: Atmospheres*, 108, 1–21, <https://doi.org/10.1029/2001jd001515>, 2003b.
- Findell, K. L., Gentine, P., Lintner, B. R., and Kerr, C.: Probability of afternoon precipitation in eastern United States and Mexico enhanced  
by high evaporation, *Nature Geoscience*, 4, 434–439, <https://doi.org/10.1038/ngeo1174>, 2011.
- Findell, K. L., Gentine, P., Lintner, B. R., and Guillod, B. P.: Data Length Requirements for Observational Estimates of Land–Atmosphere  
Coupling Strength, *Journal of Hydrometeorology*, 16, 1615–1635, <https://doi.org/10.1175/JHM-D-14-0131.1>, 2015.
- 315 Findell, K. L., Keys, P. W., van der Ent, R. J., Lintner, B. R., Berg, A., and Krasting, J. P.: Rising Temperatures Increase Importance of  
Oceanic Evaporation as a Source for Continental Precipitation, *Journal of Climate*, 32, 7713–7726, <https://doi.org/10.1175/JCLI-D-19-0145.1>, 2019.
- Georgakakos, K. P. and Bras, R. L.: A hydrologically useful station precipitation model: 1. Formulation, *Water Resources Research*, 20,  
1585–1596, <https://doi.org/10.1029/WR020i01p01585>, 1984.



- 320 Guillod, B. P., Orlowsky, B., Miralles, D., Teuling, A. J., Blanken, P. D., Buchmann, N., Ciais, P., Ek, M., Findell, K. L., Gentine, P., Lintner, B. R., Scott, R. L., den Hurk, B. V., and Seneviratne, S. I.: Land-surface controls on afternoon precipitation diagnosed from observational data: uncertainties and confounding factors, *Atmospheric Chemistry and Physics*, 14, 8343–8367, <https://doi.org/10.5194/acp-14-8343-2014>, 2014.
- Guillod, B. P., Orlowsky, B., Miralles, D. G., Teuling, A. J., and Seneviratne, S. I.: Reconciling spatial and temporal soil moisture effects on  
325 afternoon rainfall, *Nature Communications*, 6, 6443, <https://doi.org/10.1038/ncomms7443>, 2015.
- Guo, Z., Dirmeyer, P. A., and Delsole, T.: Land surface impacts on subseasonal and seasonal predictability, *Geophysical Research Letters*, 38, <https://doi.org/10.1029/2011GL049945>, 2011.
- Guo, Z. C., Dirmeyer, P. A., Koster, R., Sud, Y. C., Bonan, G., Oleson, K. W., Chan, E., Verseghy, D., Cox, P., Gordon, C. T., McGregor, J. L., Kanae, S., Kowalczyk, E., Lawrence, D., Liu, P., Mocko, D., Lu, C. H., Mitchell, K., Malyshev, S., McAvaney, B., Oki, T., Yamada,  
330 T., Pitman, A., Taylor, C. M., Vasic, R., and Xue, Y. K.: GLACE: The Global Land–Atmosphere Coupling Experiment. Part II: Analysis, *Journal of Hydrometeorology*, 7, 611–625, <https://doi.org/10.1175/JHM511.1>, 2006.
- Hersbach, H., Bell, B., Berrisford, P., Biavati, G., Horanyi, A., Sabater, J. M., Nicolas, J., Peubey, C., Radu, R., Rozum, I., Schepers, D., Simmons, A., Soci, C., Dee, D., and Thepaut, J.-N.: ERA5 hourly data on pressure levels from 1979 to present, <https://doi.org/10.24381/cds.adbb2d47>, 2018.
- 335 Hersbach, H., Bell, B., Berrisford, P., Hirahara, S., Horányi, A., Muñoz-Sabater, J., Nicolas, J., Peubey, C., Radu, R., Schepers, D., Simmons, A., Soci, C., Abdalla, S., Abellan, X., Balsamo, G., Bechtold, P., Biavati, G., Bidlot, J., Bonavita, M., Chiara, G. D., Dahlgren, P., Dee, D., Diamantakis, M., Dragani, R., Flemming, J., Forbes, R., Fuentes, M., Geer, A., Haimberger, L., Healy, S., Hogan, R. J., Hólm, E., Janisková, M., Keeley, S., Laloyaux, P., Lopez, P., Lupu, C., Radnoti, G., de Rosnay, P., Rozum, I., Vamborg, F., Villaume, S., and Thépaut, J. N.: The ERA5 global reanalysis, *Quarterly Journal of the Royal Meteorological Society*, 146, 1999–2049,  
340 <https://doi.org/10.1002/qj.3803>, 2020.
- Hu, H., Leung, L. R., and Feng, Z.: Early warm-season mesoscale convective systems dominate soil moisture–precipitation feedback for summer rainfall in central United States, *Proceedings of the National Academy of Sciences*, 118, e2105260118, <https://doi.org/10.1073/pnas.2105260118>, 2021.
- Humphrey, V., Berg, A., Ciais, P., Gentine, P., Jung, M., Reichstein, M., Seneviratne, S. I., and Frankenberg, C.: Soil moisture–atmosphere  
345 feedback dominates land carbon uptake variability, *Nature*, 592, 65–69, <https://doi.org/10.1038/s41586-021-03325-5>, 2021.
- Jach, L., Schwitalla, T., Branch, O., Warrach-Sagi, K., and Wulfmeyer, V.: Sensitivity of land–atmosphere coupling strength to changing atmospheric temperature and moisture over Europe, *Earth System Dynamics*, 13, 109–132, <https://doi.org/10.5194/esd-13-109-2022>.
- Klein, C. and Taylor, C. M.: Dry soils can intensify mesoscale convective systems, *Proceedings of the National Academy of Sciences of the United States of America*, 117, 21 132–21 137, <https://doi.org/10.1073/pnas.2007998117>, 2020.
- 350 Koster, R. D., Dirmeyer, P. A., Guo, Z., Bonan, G., Chan, E., Cox, P., Gordon, C. T., Kanae, S., Kowalczyk, E., Lawrence, D., Liu, P., Lu, C. H., Malyshev, S., McAvaney, B., Mitchell, K., Mocko, D., Oki, T., Oleson, K., Pitman, A., Sud, Y. C., Taylor, C. M., Verseghy, D., Vasic, R., Xue, Y., and Yamada, T.: Regions of strong coupling between soil moisture and precipitation, *Science*, 305, 1138–1140, <https://doi.org/10.1126/science.1100217>, 2004.
- Koster, R. D., Sud, Y. C., Guo, Z. C., Dirmeyer, P. A., Bonan, G., Oleson, K. W., Chan, E., Verseghy, D., Cox, P., Davies, H., Kowalczyk,  
355 E., Gordon, C. T., Kanae, S., Lawrence, D., Liu, P., Mocko, D., Lu, C. H., Mitchell, K., Malyshev, S., McAvaney, B., Oki, T., Yamada, T., Pitman, A., Taylor, C. M., Vasic, R., and Xue, Y. K.: GLACE: The Global Land–Atmosphere Coupling Experiment. Part I: Overview, *Journal of Hydrometeorology*, 7, 590–610, <https://doi.org/10.1175/JHM510.1>, 2006.



- Laguë, M. M., Bonan, G. B., and Swann, A. L. S.: Separating the Impact of Individual Land Surface Properties on the Terrestrial Surface Energy Budget in both the Coupled and Uncoupled Land–Atmosphere System, *Journal of Climate*, 32, 5725–5744, <https://doi.org/10.1175/JCLI-D-18-0812.1>, 2019.
- 360 Lorenz, R., Pitman, A. J., Hirsch, A. L., and Sribnovsky, J.: Intraseasonal versus interannual measures of land-atmosphere coupling strength in a global climate model: GLACE-1 versus GLACE-CMIP5 experiments in ACCESS1.3b, *Journal of Hydrometeorology*, 16, 2276–2295, <https://doi.org/10.1175/JHM-D-14-0206.1>, 2015.
- Miralles, D. G., Gentine, P., Seneviratne, S. I., and Teuling, A. J.: Land-atmospheric feedbacks during droughts and heatwaves: state of the science and current challenges, *Annals of the New York Academy of Sciences*, 1436, 19–35, <https://doi.org/10.1111/nyas.13912>, 2019.
- 365 Santanello, J. A., Peters-Lidard, C. D., Kumar, S. V., Alonge, C., and Tao, W. K.: A Modeling and Observational Framework for Diagnosing Local Land–Atmosphere Coupling on Diurnal Time Scales, *Journal of Hydrometeorology*, 10, 577–599, <https://doi.org/10.1175/2009JHM1066.1>, 2009.
- Santanello, J. A., Dirmeyer, P. A., Ferguson, C. R., Findell, K. L., Tawfik, A. B., Berg, A., Ek, M., Gentine, P., Guillod, B. P., van Heerwaarden, C., Roundy, J., and Wulfmeyer, V.: Land–Atmosphere Interactions: The LoCo Perspective, *Bulletin of the American Meteorological Society*, 99, 1253–1272, <https://doi.org/10.1175/BAMS-D-17-0001.1>, 2018.
- 370 Schumacher, D. L., Keune, J., van Heerwaarden, C. C., de Arellano, J. V.-G., Teuling, A. J., and Miralles, D. G.: Amplification of mega-heatwaves through heat torrents fuelled by upwind drought, *Nature Geoscience*, 12, 712–717, <https://doi.org/10.1038/s41561-019-0431-6>, 2019.
- 375 Seneviratne, S. I., Corti, T., Davin, E. L., Hirschi, M., Jaeger, E. B., Lehner, I., Orlowsky, B., and Teuling, A. J.: Investigating soil moisture–climate interactions in a changing climate: A review, *Earth-Science Reviews*, 99, 125–161, <https://doi.org/10.1016/j.earscirev.2010.02.004>, 2010.
- Tawfik, A. B. and Dirmeyer, P. A.: A process-based framework for quantifying the atmospheric preconditioning of surface-triggered convection, *Geophysical Research Letters*, 41, 173–178, <https://doi.org/10.1002/2013GL057984>, 2014.
- 380 Taylor, C. M., de Jeu, R. A. M., Guichard, F., Harris, P. P., and Dorigo, W. A.: Afternoon rain more likely over drier soils, *Nature*, 489, 423–426, <https://doi.org/10.1038/nature11377>, 2012.
- Taylor, C. M., Belušić, D., Guichard, F., Parker, D. J., Vischel, T., Bock, O., Harris, P. P., Janicot, S., Klein, C., and Panthou, G.: Frequency of extreme Sahelian storms tripled since 1982 in satellite observations, *Nature*, 544, 475–478, <https://doi.org/10.1038/nature22069>, 2017.
- 385 Warszawski, L., Frieler, K., Huber, V., Piontek, F., Serdeczny, O., and Schewe, J.: The Inter-Sectoral Impact Model Intercomparison Project (ISI-MIP): Project framework, *Proceedings of the National Academy of Sciences*, 111, 3228–3232, <https://doi.org/10.1073/pnas.1312330110>, 2014.
- Zhou, S., Williams, A. P., Lintner, B. R., Berg, A. M., Zhang, Y., Keenan, T. F., Cook, B. I., Hagemann, S., Seneviratne, S. I., and Gentine, P.: Soil moisture–atmosphere feedbacks mitigate declining water availability in drylands, *Nature Climate Change*, <https://doi.org/10.1038/s41558-020-00945-z>, 2021.

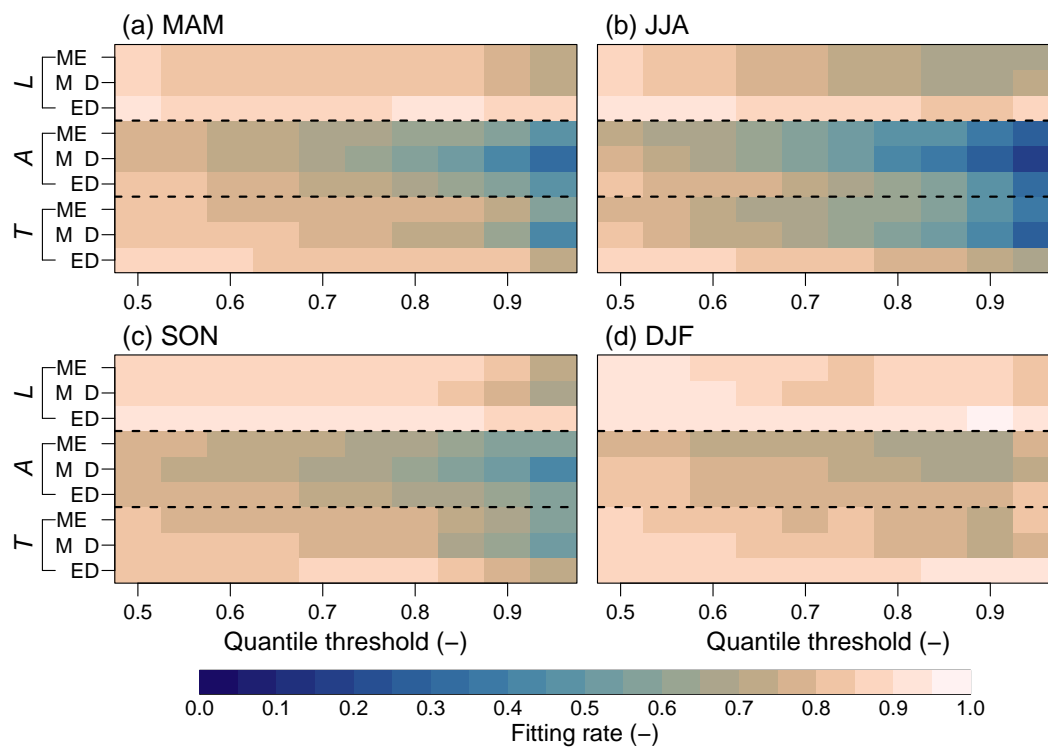


**Figure 1.** Fitting rates of different paired comparisons as a function of quantile threshold by using global data (see Sect. 2.3). The subplots represent different seasons. The three bands (separated by dashed lines) in each subplot indicate the land leg ( $\mathcal{L}$ ), the atmospheric leg ( $\mathcal{A}$ ), and the total ( $\mathcal{T}$ ). Within each band; the three rows represent three paired comparisons, they are (from top to bottom) M vs E, M vs D, and E vs D.

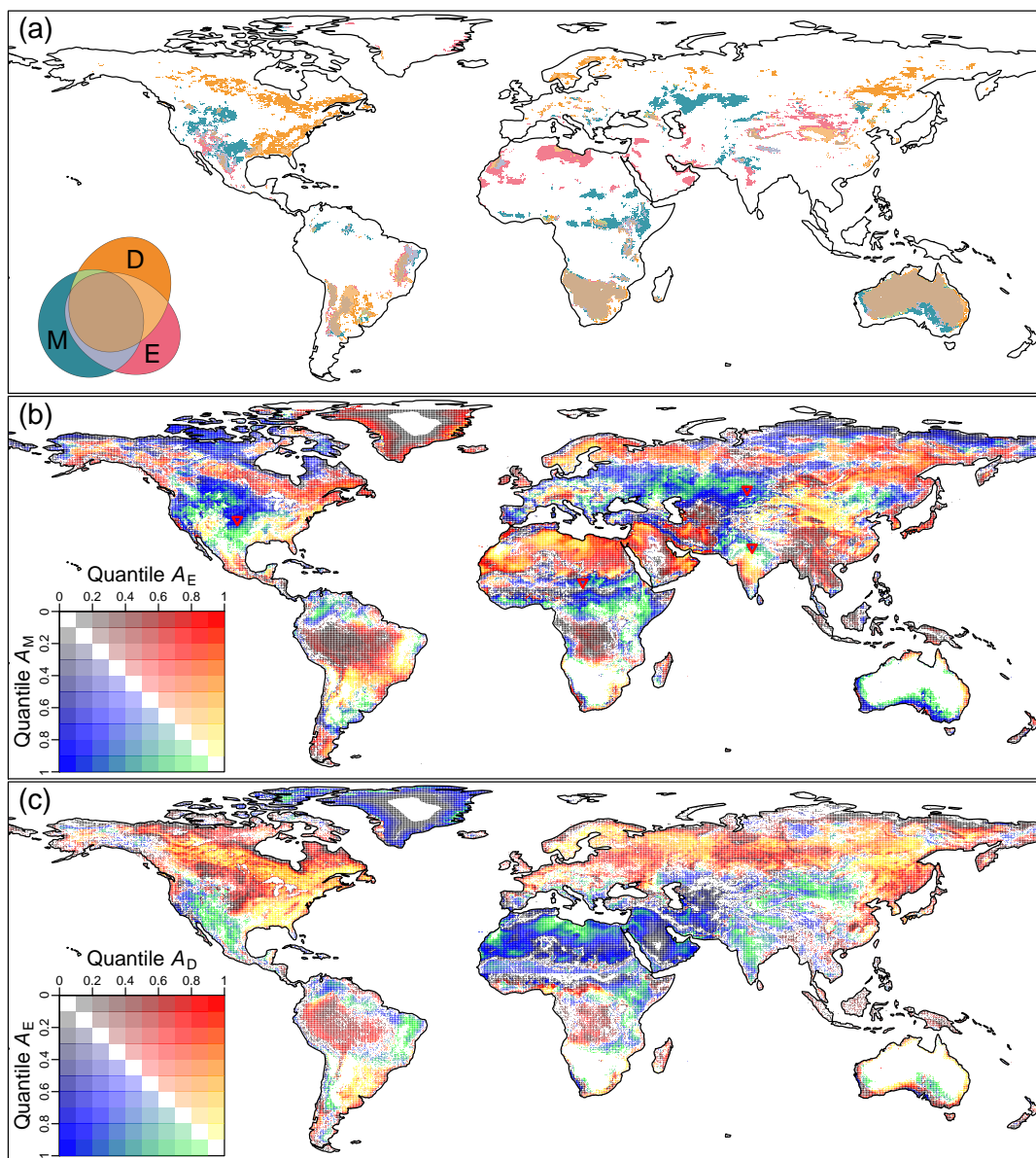


**Figure 2.** (a) Spatial patterns of significant  $\mathcal{A}_M$ ,  $\mathcal{A}_E$ , and  $\mathcal{A}_D$  (top 10% quantile of absolute values) in summer. Euler diagrams show the colors for specific relationships (intersections, unions, or disjoint) among  $\mathcal{A}_M$ ,  $\mathcal{A}_E$ , and  $\mathcal{A}_D$ , and the areas of colored patterns also correspond to the fractions. (b)-(c) Quantile changes (b) from  $\mathcal{A}_M$  to  $\mathcal{A}_E$  and (c) from  $\mathcal{A}_E$  to  $\mathcal{A}_D$  in summer. The quantile of the  $\mathcal{A}$  is separated into ten bins. The color of the grid cell is explained by the legend, where  $x$ - and  $y$ -axes indicate its quantile bins of specific  $\mathcal{A}$ . The diagram has three aspects of information. First, warm (cold) colors indicate quantile increase (decrease) from the original  $\mathcal{A}$  ( $y$ -axis) to the final  $\mathcal{A}$  ( $x$ -axis). Second, the smaller the quantile difference is, the more transparent the color. White indicates no change of quantile bin. Third, as the shifts in the large quantile bins are the main focus, we highlight this part in green and yellow. For shifts that occur within the low quantile bins, colors fade to gray. Three red triangles are samples from three regions where  $\mathcal{A}$  is dramatically underestimated by monthly smoothing.

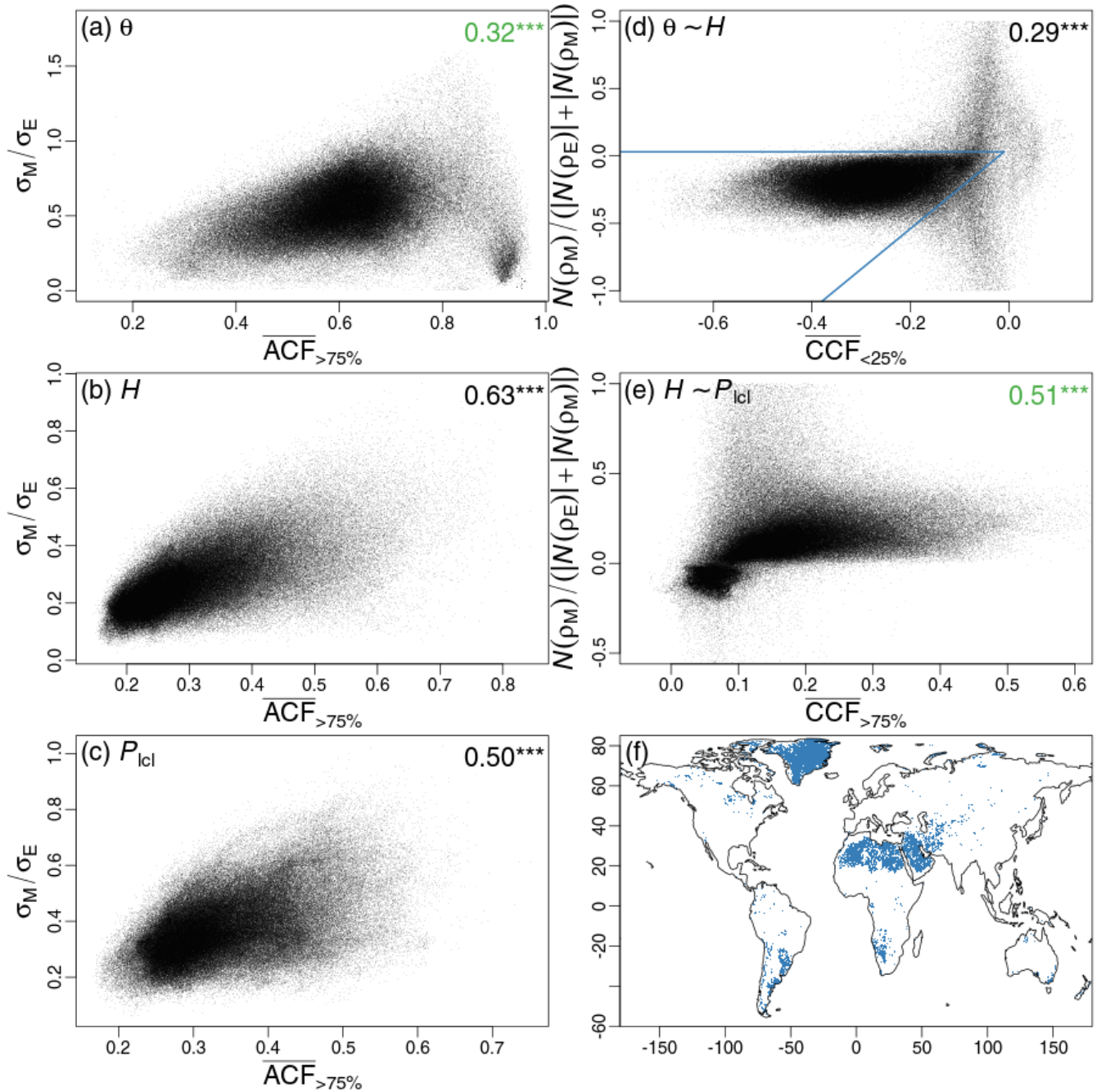


**Figure 3.** Scatter plot of coupling signal loss rate when moving from  $TLM_E$  to  $TLM_M$  as a function of an indicator reflecting the memory of L-A states. Points represent terrestrial grid cells around the globe. (a)–(c) Loss rate of the  $\sigma$  term as a function of averaged auto-correlation function ( $\overline{ACF}$ ) with quantile larger than 75% (see Sect. 2.4). (d)–(e) Loss rate of the numerator of the  $\rho$  term (see Sect. 2.4) as a function of averaged cross-covariance function ( $\overline{CCF}$ ) within a certain quantile range (shown by the subscript, see Sect. 2.4). Dark and green values at the top right are Person and Spearman correlation coefficients for linear and nonlinear relationships, respectively. \*\*\* indicates  $p < 0.001$ . (f) Patterns with values out of the main cluster (separated by two blue lines) in (e).



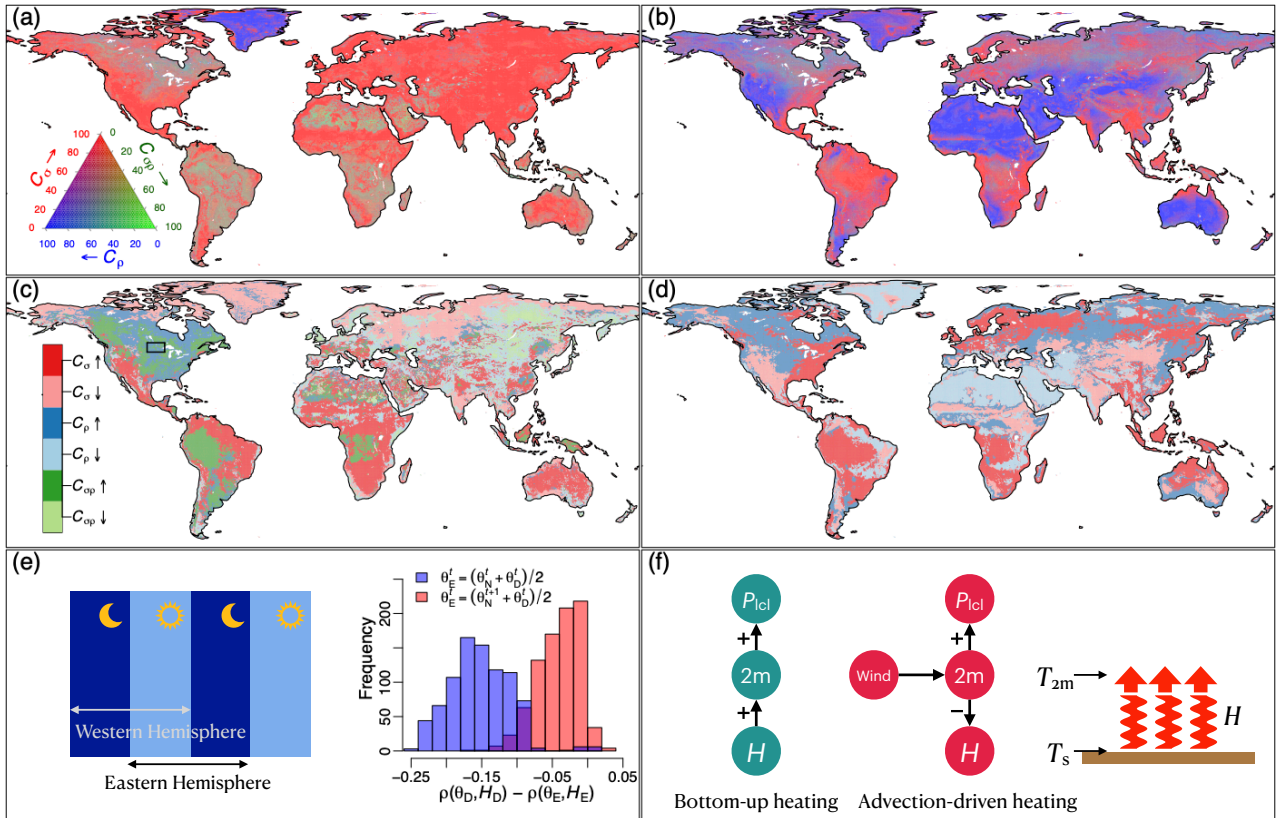


**Figure 4.** Comparison between  $TLM_D$  and  $TLM_E$ . Left panel: the land leg ( $\mathcal{L}$ ); right pane: the atmospheric leg ( $\mathcal{A}$ ). Top row: fractions of the three components of  $\Delta|M|$  ( $|M_D| - |M_E|$ , Eqs. 4 and 5, see Sect. 2.5). Red, blue, and green indicate contributions of fluctuation, correlation, and joint of the two ( $|C_\sigma|$ ,  $|C_\rho|$ , and  $|C_{\sigma\rho}$ ), respectively (see Sect. 2.5). Middle row: primary contributor to pattern shift in TLM (see Sect. 2.6). The legend contains three pairs of colors: red, blue, and green indicate  $C_\sigma$ ,  $C_\rho$ , and  $C_{\sigma\rho}$  as the primary contributor, respectively. A darker (lighter) color indicates a quantile increase (decrease) from E to D. Left panel of (e): conceptual figure showing the combinations of daytime and nighttime that make up the E time series in the Eastern versus Western Hemisphere. Right panel of (e): histograms of the difference between D- and E-based  $\rho(\theta, H)$ . Data is from the rectangle region shown in (c). The blue histogram indicates the cases with the original  $\theta_E$  (an average of the nighttime soil moisture  $\theta_N$  and the following daytime soil moisture  $\theta_D$ ). Red histogram indicates the cases with the modified  $\theta_E$  (an average of the  $\theta_D$  and the following  $\theta_N$ ). Left and middle panel of (f): two mechanisms driving the  $\mathcal{A}$ . Right panel of (f): the definition of sensible heat flux  $H$  which reflects the temperature gradient from the surface to the near-surface (2m).